Chung *et al. Radiation Oncology* (2025) 20:96
https://doi.org/10.1186/s13014-025-02673-0

Radiation Oncology

RESEARCH Open Access

Dynamic profiles of early biological responses to predict the treatment efficacy of proton therapy in liver cancer assessed with in vivo kinetic [18F]-FDG PET/MRI

Yi-Hsiu Chung[1], I-Chun Cho[2,3], Fujie Jhang[1], Chi-Chang Weng[4], Gigin Lin[5], Ching-Fang Yu[4,6*†] and Fang-Hsin Chen[7,8*†]

Abstract

Background Proton beam therapy is an advanced treatment for patients with unresectable hepatocellular carcinoma. However, evaluating the response to treatment with tumor size alone is insufficient. Herein, we used kinetic [18F]-FDG PET and diffusion-weighted MR imaging to monitor the biological responses to proton beam therapy in hepatocellular carcinoma mice to assess treatment efficacy. Murine BNL HCC cells were orthotopically implanted into the livers of 8-week-old male BALB/c mice, which received 20 Gy of the single dose in proton beam therapy. The biological responses to proton beam therapy were assessed on pre-treatment and post-treatment days 1, 3, and 7.

Results Compared with the not-receiving proton beam therapy group, the treated group led to an increasing trend in tumor K1 values and constant relative SUVs within 7 days on the dynamic PET imaging. On diffusion-weighted MR imaging, the tumor relative apparent diffusion coefficient values significantly increased post-treatment days 3 and 7. Significantly decreased tumor proliferation, cellular density, and cellular uptake of [18F]-FDG on days 1 and/or 3 post-treatment, with a rebound on day 7, were observed in the dynamic profiling of tumor cells ex vivo and in vitro. Vascular remodeling and elevated macrophage infiltrates in the tumor microenvironment were associated with proton beam therapy. However, there were no significant changes in tumor size between the treated and non-treated groups after treatment until day 7.

Conclusions In vivo kinetic [18F]-FDG PET/MRI techniques can provide a feasible means to assess early liver tumor response to proton beam therapy and predict treatment outcomes.

Keywords Proton beam therapy, Liver cancer, PET/MRI, Animal study

†Ching-Fang Yu and Fang-Hsin Chen contributed equally to this work.

*Correspondence:
Ching-Fang Yu
chingfang@mail.cgu.edu.tw
Fang-Hsin Chen
fanghsin@mx.nthu.edu.tw

Full list of author information is available at the end of the article

Introduction

Liver cancer is the third leading cause of death worldwide and the second leading cause of death in Taiwan [1, 2]. Many treatment strategies for liver cancer have been employed in clinical practice. If surgery is contraindicated, alternative treatments, including chemotherapy, immunotherapy, targeted therapy, and radiation therapy, should generally be considered [3].

Research has shown that proton beam therapy (PBT) may offer more benefits than traditional *X-ray* treatment (XRT). The unique properties of protons allow for reduced exposure to normal tissues surrounding the target area, leading to better local control and survival rates, reduced toxicity, and improved overall patient quality of life [4]. However, questions have been raised about the cost-effectiveness of patient treatment [5]. The effectiveness of PBT is usually evaluated after the completion of the treatment course. However, due to patient positioning, particle ranges, tumor size, and the heterogeneity of patient characteristics, there is uncertainty regarding the effectiveness of treatment for patients who have undergone PBT [6, 7]. To achieve precision medicine, the treatment plan for each individual must be established in a timely manner for a better outcome [8].

Animal experiments are often conducted to investigate treatment responses to and the biological effects of PBT. However, researchers must carefully consider the timing of evaluating PBT efficacy in vivo, as improper timing can result in misleading information. Notably, the dynamic biological response to PBT in vivo is limited [9–11]. Tumor size changes are often widely used as a standard for assessing the effectiveness of cancer treatments [12]. However, changes in tumor volume tend to occur at a slower rate than do changes in molecules and metabolites [13]. Molecular imaging can address this issue—it is a noninvasive tool that can help quantify changes in tumor biology during treatment in a longitudinal way [14].

[18F]- fluorodeoxyglucose (FDG)-positron emission tomography (PET) scans are utilized in the clinic for cancer diagnosis, tumor staging, and prognosis prediction [15]. This technique provides quantified metabolic information on tumors using the glucose analog [18F]-FDG. The standardized uptake value (SUV) is a commonly used parameter in clinical imaging for the semiquantitative assessment of lesion uptake. However, SUV is dependent on several factors, such as the time interval between injection and scanning, the settings for image acquisition and correction, and the reconstruction algorithm used. These factors should be considered when interpreting SUV values [16]. Dynamic [18F]-FDG PET scans have become more feasible in recent years, as whole-body scans are now possible. With adequate kinetic modeling for a tracer, dynamic PET scans can aid in understanding the pathology and biological process of a lesion [16]. The distribution and metabolic process of [18F]-FDG from blood vessels to phosphorylation were established based on a two-compartment model [17]. The imaging-derived parameters used in this context are K1, k2, and k3. K1 represents the one-way flow of [18F]-FDG from blood vessels to tumor microenvironment cells; k2 represents the rate of transportation of [18F]-FDG from cells to blood vessels; and k3 represents the rate of intracellular [18F]-FDG phosphorylation to FDG-6-P (18 F-FDG-6-phosphate). The relationships between these parameters are determined by the equation ki (net tracer influx constant) = (K1 x k3)/(k2 + k3). K1, in particular, is correlated with vessel perfusion in the tumor microenvironment. k3 and ki are associated with tumor glycolysis. These imaging parameters have been investigated for their relationship with tumor characterization and treatment [11, 18].

Diffusion-weighted imaging (DWI) is based on measuring the diffusion of water molecules in tissue by magnetic resonance imaging (MRI). The apparent diffusion coefficient (ADC) value derived from DWI is highly correlated with tissue properties such as the size of the extracellular space, viscosity, and cellularity [19]. One study showed that changes in the ADC on early MRI were closely related to in-field control in patients with hepatocellular carcinoma (HCC) treated with stereotactic ablative radiotherapy [20]. Consistently, in our previous report, the ADC of liver tumors was significantly higher in the XRT group than in the non-irradiation group [10]. ADC has also been reported to be negatively correlated with cell density and the cellular proliferation rate in HCC patients [21].

The primary goal of this study was to establish a multi-imaging platform to explore the dynamic profiles of tumor biological reactions to PBT in orthotopic HCC mice. This goal was achieved by conducting in vivo kinetic [18F]-FDG PET/MRI and validated through ex vivo histopathological analysis and in vitro cellular studies. The ultimate aim of this research was to validate the use of imaging parameters as predictors of early treatment response in patients with HCC.

Materials and methods

Experimental design

This study included in vivo imaging and ex vivo studies to investigate the changes in irradiated tumors before and at different time points after PBT treatment. All mice were screened using bioluminescence imaging before irradiation to ensure tumor development. T2-weighted MRI was used to determine the size of the tumor, reaching approximately 5 mm in diameter over a period of eleven days for further PBT with 20 Gy. In vivo [18F]-FDG PET/DWI of tumor-bearing mice was conducted before and after PBT on days 1, 3 and 7. Independent ex vivo

histopathological studies and in vitro [18F]-FDG cellular uptake studies were performed to validate the in vivo imaging results on specific days. The experimental flow chart is shown in Fig. 1. All animal proton irradiation and in vivo image acquisition protocols followed the animal guidelines established and approved by the Institutional Animal Care and Use Committee of Chang Gung Memorial Hospital, Taiwan (IACUC 2022010302).

Cell culture and animal model

The procedures used for cell culture and animal model establishment were described in a previous study [10]. The BNL 1ME A.7R.1 murine HCC cell line, which expresses the firefly luciferase gene, was maintained in Dulbecco's modified Eagle's medium supplemented with 10% fetal bovine serum and 1% penicillin/streptomycin (all reagents from Gibco, Thermo Fisher Scientific, Inc., Waltham, MA) and incubated at 37 °C in humidified air containing 5% CO_2. Murine BNL HCC cells were orthotopically implanted into the livers of 8-week-old male BALB/c mice. Anesthesia was induced using 2% isoflurane, and median laparotomy was performed to expose the surface of the right liver lobe. The BNL HCC cells were suspended in 10 μL of culture medium mixed with Matrigel (1:1) and injected into the subcapsular region of the liver using a 30-G needle.

Proton irradiation

During proton irradiation, the mice were anesthetized using a 1:1 mixture of ketamine (50 mg/mL) and 1% xylazine (Rompun) and were securely restrained in a custom holder using adhesive tape. Each mouse was placed in a vertical supine position with the xiphoid process centered among the abdominal quadrants and a noticeable small bump located in the left upper quadrant. Proton irradiation was performed at the Radiological Research Core Laboratory of Linkou Chang Gung Memorial Hospital. A proton beam with an energy of 230 MeV and a dose rate of 0.4 Gy/s was used for all irradiations. A pencil beam scanning system was utilized for in vivo mouse proton therapy. The beam was collimated to a 10 mm × 10 mm field and centered over the visible tumor bump, covering a total field of view of approximately 11 mm × 13 mm in the left upper abdominal quadrant. The right hepatic lobe received a targeted dose of 20 Gy, delivered via a clinical cyclotron system. Supplemental data 1 provides detailed information on the radiation dose of the field-of-view profile during proton beam irradiation. For in vitro experiments, suspended cells in Eppendorf tubes were irradiated with a 3 Gy dose at the center of the spread-out Bragg peak (SOBP), generated using a broad proton beamline. The dose-averaged linear energy transfer (LETd) at the target region was approximately 2–3 keV/μm [22].

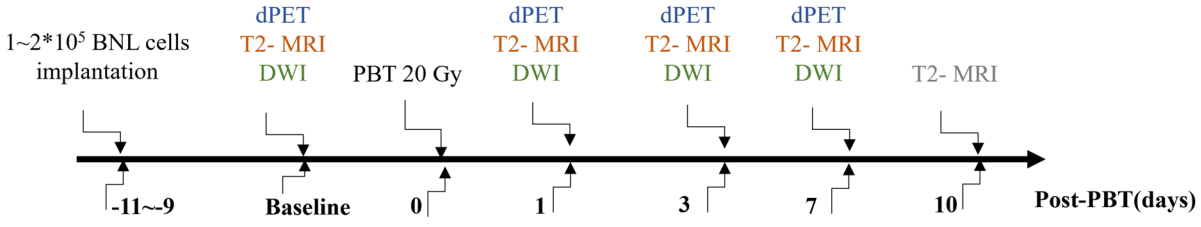

Methodology	Grouping and animal numbers	Comparison (non-parametric t-test)
Imaging parameters • sPET-derived SUV • dPET-derived K1, ki, k3 • T2- MRI-derived tumor size • DWI-derived ADC	Non-PBT (n =6, except day 7, n=4) and PBT (n =6) groups Non-PBT (n =4) and PBT (n =4) groups Non-PBT (n =5) and PBT (n =4) groups	• Compared with its baseline for individual group (#) • Non-PBT v.s. post-PBT on days 1,3 and 7 (*)
Ex vivo tissue study • H&E • IHC: Ki-67 • IHC-F : CD31, F4/80 • WB: Glut1, HK1	Non-PBT (n=3) and PBT (n=3) groups	• Non-PBT v.s. post-PBT on days 1,3 and 7
In vitro cellular uptake • [18F]-FDG	Non-PBT (n=6) and PBT(n=6) groups	• Non-PBT v.s. post-PBT on days 1,3 and 7

Fig. 1 The experimental design and workflow. This study included in vivo imaging, ex vivo tissue staining in mice, Western blotting of cell lysates, and in vitro [18F]-FDG uptake experiments before and at various time points after proton beam therapy (PBT)

Dynamic [18F]-FDG PET scan

All mice were fasted overnight, and their glucose levels were measured with a blood glucose meter (FreeStyle Optium Neo, Abbott Diabetes Care, Ltd.) before [18F]-FDG injection. A 30-gauge needle connected to a PD-10 catheter was inserted into the lateral tail vein for further [18F]-FDG tracer administration. The animal was placed in a prone position on the animal holder of the scanner and moved to the center of the field of view after ensuring blood flow from the catheter. Mice were anesthetized with 2% isoflurane in 100% air during the PET study. All data acquisition was initiated 3 s before the tracer injections. A bolus of [18F]-FDG (8.67 ± 0.85 MBq) was manually injected through the tail vein catheter, and the net dose was corrected by subtracting the residual dose in the syringe. A 56 min dynamic image was acquired on a PET/CT scanner at the one-bed position (nanoScan PET/CT, Mediso, Hungary). The framing protocol of the dynamic PET study was 6 × 10 s, 9 × 60 s, and 10 × 300 s, and images were reconstructed with a voxel size of 0.4 mm*0.4 mm*0.4 mm via Tera-Tomo™ 3D PET iterative reconstruction via real-time Monte Carlo-based physical modeling.

PET data analysis

The liver tumor region of interests (ROIs) was defined by summing the 56 min of the framed images. First, the entire tumor was manually drawn from the coronal view, and a threshold of (maximum radioactivity minus minimum radioactivity) × 20% was applied to automatically contour the whole tumor. The image-derived input function (IDIF) was acquired from the vena cava of the mouse in the 2nd frame (10–20 s after [18F]-FDG injection). Using FDG two-compartment modeling [16, 23], the K1, k3, and ki imaging parameters were obtained. The SUVs of the tumors were obtained through semiquantitative analysis of 56-min static images.

DWI/T2 MRI

A 9.4 T magnetic resonance scanner (BioSpec 94/21USR; Bruker, Karlsruhe, Germany) was used to determine the tumor location for proton beam collimation and to monitor tumor responses following proton therapy. The abdomen of each mouse was placed in the center of the magnet. Each mouse was anesthetized with 2% isoflurane during the MRI procedure with respiration gating techniques. The parameters used for T2-weighted MRI were as follows: Bruker RARE sequence; TR/TE, 800/23 ms; slice thickness, 1 mm; slice number, 13; number of averages, 8; echo train length, 6; matrix, 256 × 256; and flip angle, 180°. The ROIs of the tumor were manually determined from transverse T2-weighted MR images. Tumor volume was determined as the maximum tumor ROI slide × slide thickness. DW-MR images were acquired using the following parameters: Bruker DtiEpi sequence; three gradient directions and two b values (0 and 1,000 s/mm^2); TR/TE, 3,000/20 ms; slice thickness, 0.8 mm; slice number, 13; number of averages, 5; matrix size, 128 × 128; flip angle, 90°; and field of view, 35 × 35 mm. The ADC values of the tumors were determined manually by the contoured ROIs of the tumors on the ADC maps derived from DWI, excluding the distorted region. All images were analyzed using PMOD version 4.004 image analysis software (PMOD Technologies LLC, Fällanden, Switzerland).

Ex vivo histopathological examination

An independent histopathological study was conducted corresponding to the timeline of the imaging study. Tumor tissues were processed via a formalin-fixed paraffin-embedded procedure and sliced into 3-μm sections, followed by hematoxylin and eosin (H&E) staining and immunohistochemistry (IHC). In the immunofluorescence (IF) study, tumor tissues were embedded in an optimal cutting temperature compound and sliced on a cryostat to generate 10-μm-thick tissue specimens. The cellular density of the tumor regions was randomly analyzed in hematoxylin-stained images in eight ROIs (TissueGnostics, Wien, Austria). Moreover, the sections were stained with primary antibodies against the following specific markers: Ki-67 (Abcam, Cambridge, UK), F4/80 (Bid-Rad, Hercules, CA), and CD31 (BD Biosciences, San Jose, CA); all antibodies were used at a 1:200 dilution. IHC was conducted using DAB (HRP) kits (Abcam, Cambridge, UK), and antibodies were used at a 1:200 dilution. IF was conducted using fluorescent dye-conjugated secondary antibodies (Invitrogen, Carlsbad, CA) at a 1:100 dilution. Three tumors from each time point were included.

Western blotting

The Western blot protocol was described in a previous study [24]. The tumor samples were washed with PBS, cut into small pieces, and then lysed in Pierce™ RIPA Buffer (Thermo Fisher Scientific, Inc., Waltham, MA, USA). The tumor lysates were centrifuged, and the supernatants were harvested as protein samples. A standard curve of the total protein content was generated using Coomassie Plus™ Protein Assay Reagent (Thermo Fisher Scientific, Inc., Waltham, MA, USA). The tumor lysates were analyzed by Western blotting. The membranes were incubated with anti-glucose transporter 1 (Glut1, Abcam, Cambridge, UK) and anti-hexokinase 1 (HK1, Proteintech, Chicago, IL, USA) antibodies overnight at 4 °C. The membranes were then incubated with a horseradish peroxidase-conjugated goat anti-rabbit antibody (BioLegend, San Diego, CA). The signals were analyzed using ImageJ image processing software. The protein

expression levels of Glut1 and HK1 were quantified and normalized to that of GAPDH. Three tumors from each time point were included.

In vitro cellular uptake of [18F]-FDG

Briefly, BNL HCC cells suspended in an Eppendorf tube were positioned vertically under a collimated proton beam and subjected to a single fractionated irradiation dose of 3 Gy. After irradiation, 1×10^5 BNL HCC cells were seeded into 12-well culture plates. The methodology of the [18F]-FDG cellular uptake experiment was described in a previous study [10]. At 1, 3, and 7 days after proton irradiation, a solution of 1 μCi of [18F]-FDG in 0.5 mL of growth medium was added to the culture dishes. The cells were then incubated for 1 h at 37 °C. After incubation, the cells were washed with 1 mL of PBS to remove any unabsorbed [18F]-FDG. They were then detached by incubation with trypsin-EDTA (Gibco) for 5 minutes at 37 °C and resuspended in growth medium. The total number of cells in each sample was determined using an automatic cell counter (LunaFL™ dual fluorescence cell counter; Logos Biosystems, Gyeonggi-do, South Korea). Finally, γ-ray emission from the samples was counted at 511 keV using a Wizard 1480 Gamma Counter (Perkin Elmer, MA). All experiments were performed with six replicates. The cellular uptake of [18F]-FDG was expressed as radioactivity counts per cell.

Statistical analysis

Statistical analyses were performed using Prism software, version 8 (GraphPad, La Jolla, CA). The imaging parameter results are expressed relative to the baseline (mean ± standard deviation). The histopathological, Western blotting, and [18F]-FDG cellular uptake results are expressed as general quantified values. Two-way ANOVA with Bonferroni's multiple-comparisons tests was used for *Post hoc* analysis in vivo imaging ($n \geq 4$). Student's t test with nonparametric statistical analysis was used in vitro studies ($n = 6$) and ex vivo ($n = 3$) studies of PBT and non-PBT comparison in accordance with the Resource equation method [25]. The number of animals used in each study is listed in Fig. 1. A P value ≤ 0.05 was considered to indicate a statistically significant difference.

Results

Static and dynamic [18F]-FDG PET of HCC

Tumor-bearing mice that did or did not receive PBT were subjected to FDG PET; representative transaxial images are shown in Fig. 2a. The SUVs of the tumors were calculated from the initial injection to 56 min to generate static images. The relative SUVs were obtained from the SUV at specific time points and were normalized to the baseline value. The relative SUVs of the tumors in the group without PBT (non-PBT) increased with tumor growth (1.15 ± 0.22, 1.31 ± 0.41 and 1.56 ± 0.39 for days 1, 3 and 7, respectively) (Fig. 2b). In comparison, the relative SUVs of the irradiated tumors (PBT group) were 0.80 ± 0.16, 0.92 ± 0.20, and 0.76 ± 0.29 on post-PBT days 1, 3 and 7, respectively, indicating that the proton beam effectively controlled tumor activity (Fig. 2b). Furthermore, imaging parameters derived from the kinetic [18F]-FDG PET, i.e., K1, ki, and k3, were used for monitoring the tumor response to PBT. Compared to that of SUVs, K1, which indicates the forward transport rate constant of FDG from blood to the tumor, showed a significant decrease of 38% at the late time point in the non-PBT group. In contrast, K1 tended to increase in the PBT group (1.23 ± 0.38, 1.60 ± 0.70 and 1.70 ± 0.38 for days 1, 3 and 7, respectively) (Fig. 2c). Although there was no significant difference in the relative ki and k3 values between the PBT and non-PBT groups on the indicated days, proton irradiation treatment indeed triggered decreases in ki and k3 on day 1 of 34% and 29%, respectively, compared to the baseline values. The k3 values remained similar from day 1 to day 7 after PBT (Supplemental data 2). Taken together, these findings indicate that SUVs can be used to monitor tumor growth and that proton irradiation can inhibit tumor growth. Furthermore, kinetic imaging parameters, such as K1 and k3, indicate elevated blood perfusion in the tumor microenvironment and decreased glycolysis in tumors after PBT. These parameters could indicate valuable early biological responses to PBT.

T2-weighted MRI and DWI-derived ADC values

MRI scans were conducted to determine the sizes of the tumors and changes in water diffusion within the tumors. T2-weighted transaxial images from both the non-PBT and PBT groups were examined (Fig. 3a), and tumor sizes on days 1, 3, 7, and 10 were measured. These sizes were normalized to the sizes before irradiation, indicated as the baseline. The tumors in the non-PBT group grew rapidly, with relative changes of 3.41 ± 1.47, 6.23 ± 3.17, 9.33 ± 4.34, and 12.16 ± 5.72 on days 1, 3, 7, and 10, respectively. However, proton irradiation significantly inhibited tumor growth. In the PBT group, the relative changes were 4.34 ± 3.61, 4.22 ± 3.31, 2.82 ± 0.71* and 3.15 ± 2.81* on days 1, 3, 7, and 10, respectively (Fig. 3b). Notably, there was no significant difference in tumor size between the non-PBT and PBT groups until 7 days post irradiation (*, $p < 0.05$).

The degree of water molecular diffusion in the tumor microenvironment was also identified using ADC values on specific days and compared statistically between the non-PBT and PBT groups. In the non-PBT group, the relative ADC values of the tumors continuously decreased during growth to 0.85 ± 0.11. In contrast, in the PBT group, the relative ADC values increased after irradiation; this increase was significant on day 3 (1.2 ± 0.11,

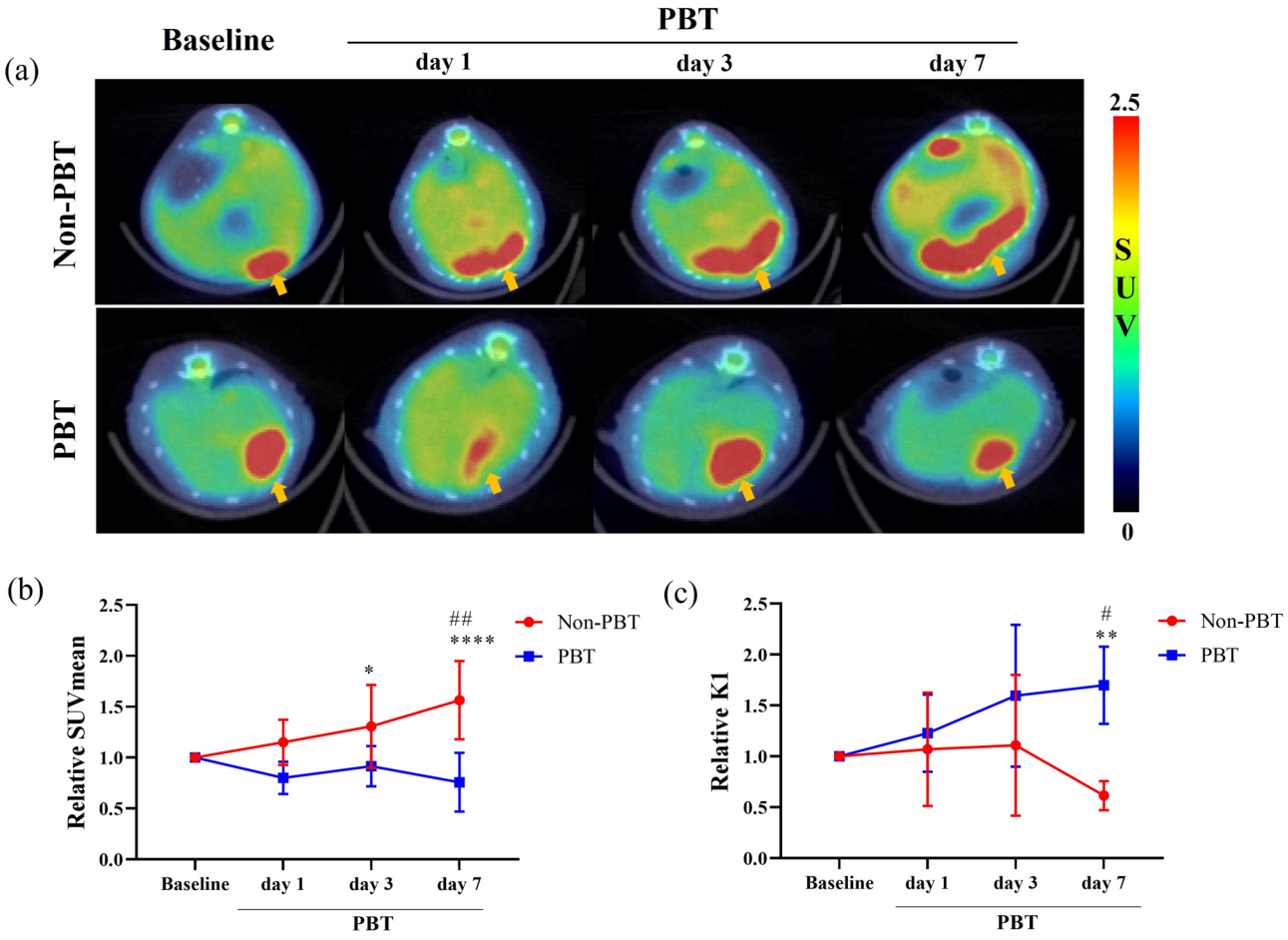

Fig. 2 The impact of PBT on [18F]-FDG uptake in orthotopic HCC tumors. **a**. Representative transaxial [18F]-FDG PET/CT images demonstrating tumor uptake in mice in the non-PBT and PBT groups before and at various time points after treatment. **b**. The changes in [18F]-FDG uptake in the tumor were calculated as the relative SUVmean (normalized to the baseline time point) over time. **c**. Changes in blood perfusion by [18F]-FDG in tumors were calculated as the relative K1 over time. The yellow arrows in the PET/CT images indicate the locations of the tumors. ($n=6$, except on day 7 for the non-PBT group, $n=4$. *, **, and **** represent p values < 0.05, < 0.01, and < 0.0001, respectively, in the non-PBT group vs. the PBT group; #, and ## denote p values < 0.05 and < 0.01, respectively, compared with the baseline of the non-PBT group.)

$p<0.0001$) and remained elevated on day 7 (1.19 ± 0.1, $p<0.001$) (Fig. 3c). Therefore, a single 20 Gy proton irradiation of orthotopic HCC tumors caused a prolonged delay in tumor growth and increased water molecular diffusion as early as 3 days after irradiation.

Effects of cellular biological changes on PBT

Ex vivo H&E staining of non-PBT and PBT tumors revealed an enlarged extracellular space and no cytoplasmic features early after irradiation. However, on day 7 after PBT, the pathological features were similar between the two groups (Fig. 4a). Compared with that in the non-PBT group, the cellular density of tumors significantly decreased on day 3 in PBT group, as indicated by the increase in the amount of extracellular space, as determined by H&E staining and cell number quantification (control: $5{,}472\pm445.1$ cell numbers/mm^2 vs. post-PBT 3 days: $4{,}226\pm573$ cell numbers/mm^2, $p<0.05$) (Fig. 4b); these findings were correlated with the increase in ADC values derived from DWI. However, the cellular density rebounded on day 7 after PBT. In addition, tumor cell proliferation was significantly reduced in the early days after PBT treatment (non-PBT: $33.05\pm7.00\%$ vs. post-PBT 1 day: $9.11\pm9.74\%$, $p<0.01$; post-PBT 3 days: $15.78\pm5.33\%$, $p<0.01$). Interestingly, there was a rebound in cell proliferation on later days (post-PBT 7 days, $28.52\pm7.52\%$) (Fig. 4c and 4). To investigate the signaling pathway involved in tumor glycolysis during proton irradiation, tumor samples were analyzed via Western blot using glycolysis-associated antibodies. Glut1 is a membrane-specific protein that is frequently present in tumor cells. Its primary role is to facilitate the transportation of glucose across the cell membrane. Once glucose is transported into the cytoplasm, the first enzyme of glycolysis, i.e., hexokinase, catalyzes the phosphorylation of glucose using ATP, resulting in the production of glucose-6-P

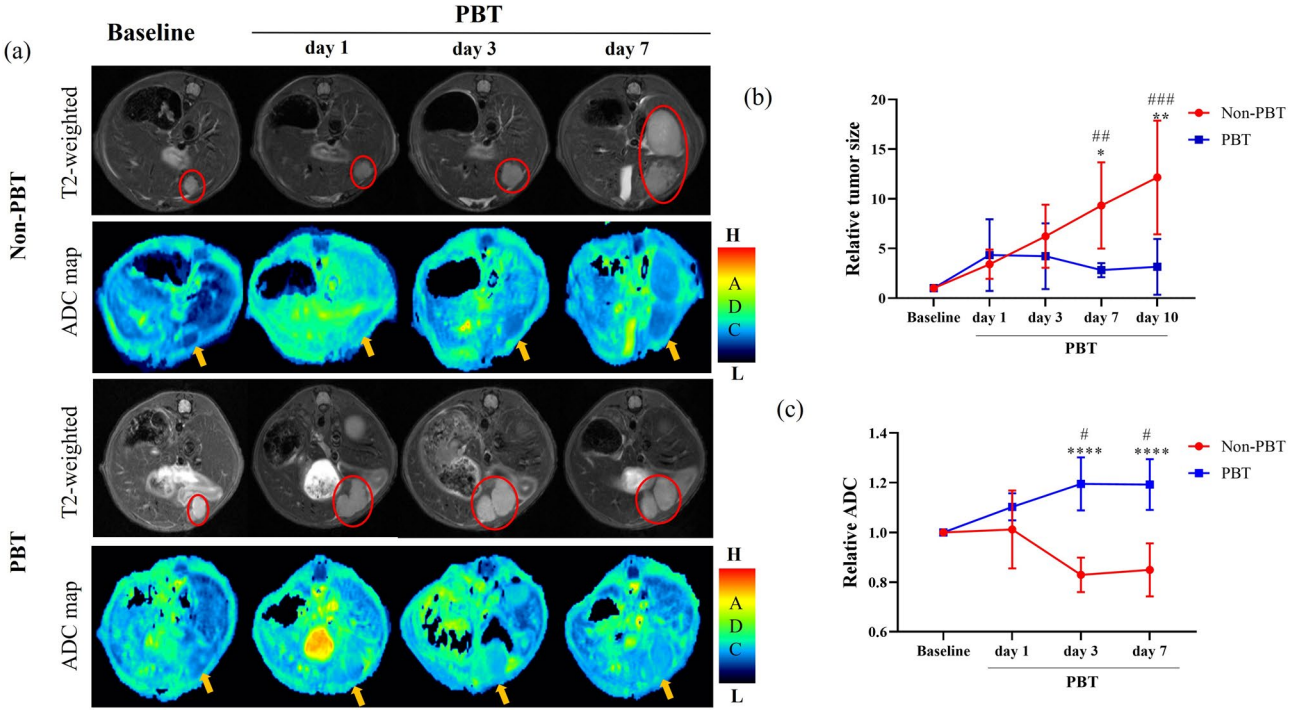

Fig. 3 The impact of PBT therapy on tumor growth and ADC values in orthotopic HCC tumors. **a**. Representative transaxial T2-weighted images and apparent diffusion coefficient (ADC) maps showing changes in the tumors on the indicated days in the non-PBT and PBT groups. **b**. The relative tumor sizes were quantified on the indicated days in both groups. **c**. The relative ADC values were measured from ADC maps on the indicated days in both groups. The tumor sites in the T2-weighted images and ADC maps are indicated by red circles and yellow arrows, respectively. ($n = 4$, *, **, and ****, $p < 0.05$, < 0.01 and < 0.0001 in the non-PBT group vs. the PBT group; #, ##, ###, $p < 0.05$, < 0.01 and < 0.001 compared with the baseline of the non-PBT group)

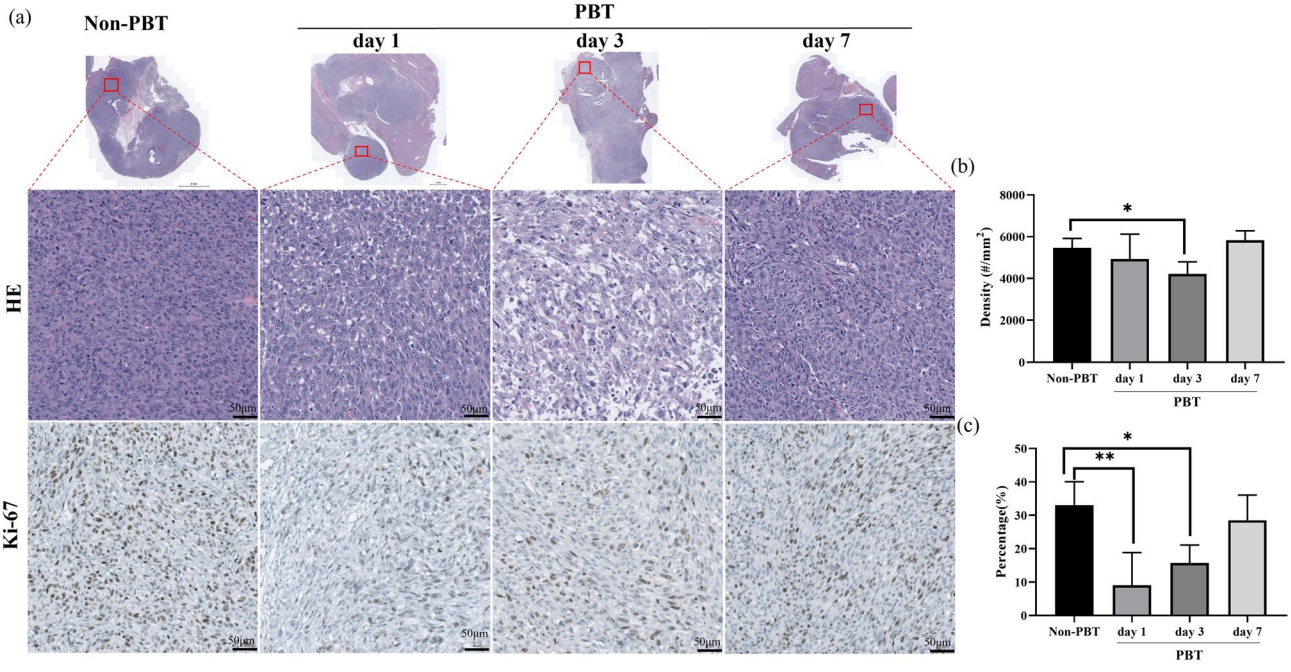

Fig. 4 The impact of PBT on tumor morphological changes and the proliferation rate of HCC tumors. **a**. Representative HE-stained sections and Ki-67 staining of non-PBT- and PBT-treated tumors (×400, scale bars 50 μm). **b**. The cellular density significantly decreased on day 3 after PBT. **c**. The proliferation rate was lowest on day 1 and rebounded on day 7 after PBT. For each tumor, at least eight fields were analyzed, $n = 3$ for each group, * and **, $p < 0.05$ and < 0.01, comparisons between the non-PBT and PBT groups)

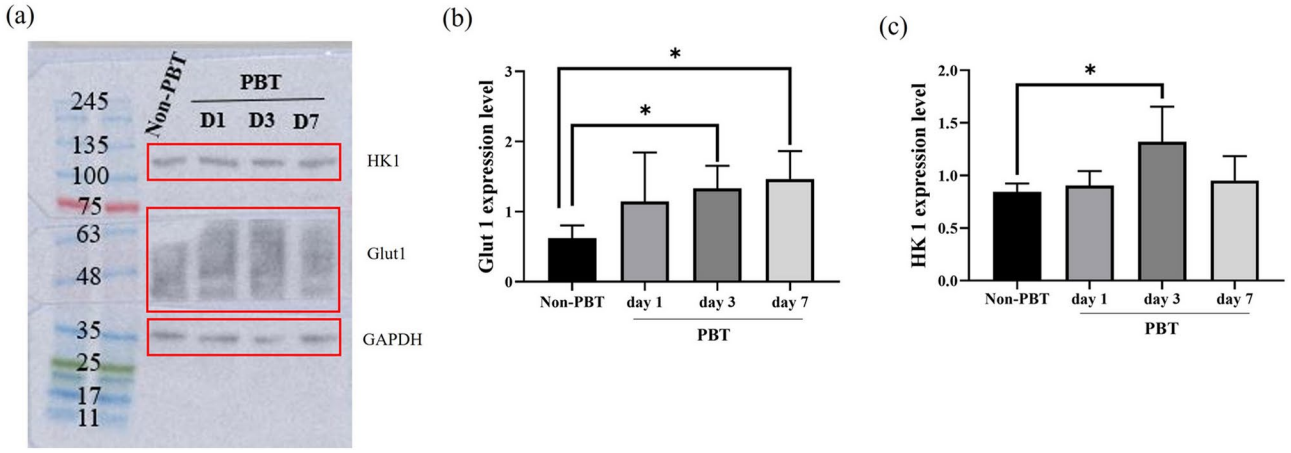

Fig. 5 The tumors that received PBT showed an increase in glycolytic metabolism. **a**. Western blot showing the expression of the Glut1 and HK1 proteins and the control protein, GAPDH, in non-PBT, post-PBT day 1, day 3, and day 7 tumor tissues. **b**. and **c**. The expression of the Glut1 and HK1 proteins significantly increased after PBT. ($n = 3$ for each group, *, $p < 0.05$, comparisons between the non-PBT and PBT groups)

Table 1 [18F]-FDG cellular uptake measured in BNL cells

Cellular uptake (Count per min/cell)	Non-PBT($n=6$)	PBT($n=6$)	*P*-value
day1	0.025 ± 0.0048	0.019 ± 0.0018	0.013*
day3	0.028 ± 0.0049	0.027 ± 0.0110	0.394
day7	0.024 ± 0.0046	0.049 ± 0.0280	0.059

Compared [18F]-FDG cellular uptake at different time points in the PBT group and the non-PBT group. The study revealed a significant decrease in cellular uptake of [18F]-FDG on post-PBT day 1 ($n=6$ for each group, *, $p<0.05$)

[26]. Alterations in Glut1 and HK1 protein expression in tumors did not occur on day 1, but at 3 and 7 days post-PBT, the levels of these two enzymes were higher in the PBT group than in the non-PBT group (Fig. 5). However, Western blot analyses cannot exclude the contribution of stromal cells, rather than tumor cells themselves, to the increased expression of Glut1 and HK1 in tumor tissues. Therefore, an in vitro experiment was conducted using BNL cells to study the effect of proton irradiation on cellular [18F]-FDG uptake. [18F]-FDG uptake was significantly lower on day 1 after proton irradiation, similar on day 3, and higher on day 7 in the irradiated group than in the nonirradiated group; however, these differences were not significant (Table 1). These data could also explain the decreasing SUV in tumors after PBT, especially in the early days after treatment. The results of this study demonstrated decreased glycolysis induced by proton irradiation, both in HCC tumors and in hepatoma cells, and increased levels of proteins associated with the glycolysis pathway. According to the in vivo [18F]-FDG PET results, the k3 value, the cell number and in vitro cellular uptake, tumor glycolysis was greatly limited on the first day and/or day 3 after PBT, but it gradually rebounded on day 7.

Histopathological alterations in the HCC tumor microenvironment

In addition to tumor cell proliferation and glycolytic status, stromal components, such as tumor vasculature and tumor-associated macrophages, were also examined to evaluate overall alterations in the tumor microenvironment. The tumor vasculature was examined with the endothelial marker CD31 to visualize the vascular structure and quantify the vascular density. In the non-PBT group, the tumor vasculature had a thin and short structure, and in the PBT group on day 7 post-irradiation, widened and extended vasculature was observed (Fig. 6a). Vascular remodeling after PBT may be related to an increase in blood perfusion and the ADC, which is a measure of the water molecular diffusion capacity in tumors and is not only associated with cellular density [27] but also the blood perfusion capability tumors [28]. There was no significant difference between the non-PBT and PBT groups in the quantified CD31 signal in tumor sections (Fig. 6b). To summarize, by integrating the cellular density and vascular remodeling results, as well as imaging parameters such as K1 and ADC values, it is possible to map changes in the tumor microenvironment after PBT in the early stages. Based on these findings, it can be concluded that within three days of PBT, the tumor microenvironment experiences a decrease in cellular density and alterations in tumor vascular structure, which result in an increase in K1 and ADC values.

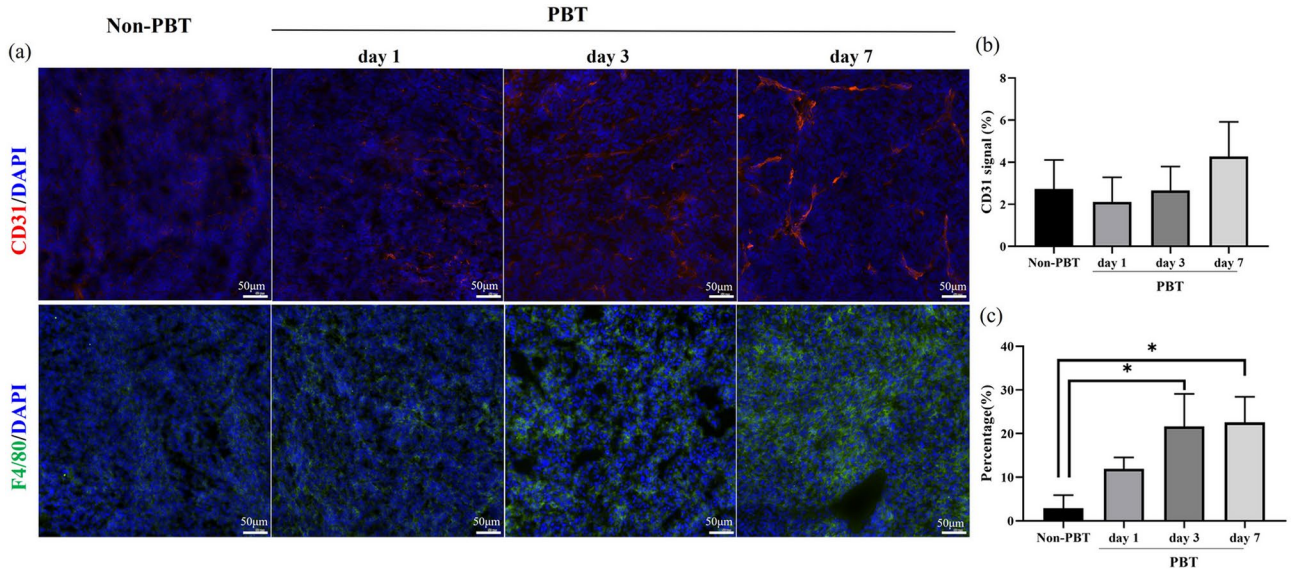

Fig. 6 The impact of PBT on vascular remodeling and macrophage infiltration in HCC tumors. **a**. Representative images of CD31 and DAPI fluorescence in non-PBT- and PBT-treated tumors are shown; the vascular structure on day 7 after PBT expanded and remodeled. Increased macrophage infiltration in PBT-treated tumors was observed by F4/80 and DAPI staining (×400, scale bars 50 μm). **b**. There were no significant changes in CD31 expression after PBT. **c**. F4/80 expression was quantified, and F4/80 was significantly elevated on days 3 and 7 after PBT. ($N = 3$ for each group, *, $p < 0.05$, comparisons between the non-PBT and PBT groups)

In a previous study, macrophages infiltrated the tumor microenvironment of an HCC tumor model after irradiation with 15 Gy XRT [10]. To explore the possible inflammatory effect of 20 Gy PBT, ex vivo tumor tissues were stained with F4/80. Figure 6c show the increased infiltration of F4/80 + macrophages into tumors on post-PBT days 3 and 7 (control: 2.87 ± 3.01%, post-PBT 1 day: 11.93 ± 2.60%; post-PBT 3 days: 21.94 ± 7.46%; post-PBT 7 days: 22.55 ± 5.87%; *, $p < 0.05$). The infiltration of macrophages did not interfere with the SUV to cause false-positive signals. However, macrophage infiltration might partially contribute to the increased expression of Glut1 and HK1 at late time points.

Discussion

The findings from this study indicate that PBT can effectively reduce tumor glycolysis and proliferation, promote blood perfusion and increase the diffusion of water molecules in surrounding tissue, ultimately leading to the suppression of tumor growth in HCC models 7 days after treatment. These results were obtained through the use of integrated dynamic [18F]-FDG PET and functional MR images. On the first day after proton irradiation, PBT dramatically reduced glycolysis in HCC cells, as suggested by [18F]-FDG PET images and cellular uptake experiments, the results of which indicated possible cell death and a decrease in the tumor proliferation rate. Additionally, there was a noteworthy trend toward increased ADC values from DWI-MRI and K1 from [18F]-FDG PET following PBT. This trend indicated that the diffusion of water molecules and the perfusion capability of the tumor microenvironment increased. These findings were validated by ex vivo tissue analysis of the tumor cell density and proliferation indices (Ki-67 and CD31 expression). Moreover, the constant SUV after PBT may be linked to the balance between the increase in macrophage infiltration and the decrease in the numbers of living tumor cells. In addition, the expression levels of Glut1 and HK1 in tumor tissues were elevated on days 3 and 7, which might also account for the increased SUVs in the PBT group. Our study revealed that kinetic imaging parameters, specifically K1 and k3, derived from dynamic [18F]-FDG PET, as well as the ADC derived from DWI-MRI, can provide insight into tumor glycolysis, water diffusion, and blood perfusion capabilities after proton beam therapy for HCC prior to any visible morphological changes. Based on early biological responses to PBT, it can be proposed that combining therapies, such as targeting angiogenesis and glycolysis in combination with PBT, could have synergistic effects in early HCC treatment.

Proton vs. X-ray treatment response in liver cancer

PBT offers several advantages over XRT for treating liver cancer. One of the most notable benefits of PBT is its ability to reduce liver toxicity. A study by Cheng et al. revealed that the risk of radiation-induced liver disease was significantly lower in a PBT group than in an XRT group (11.8% vs. 36%, $p = 0.004$) [29]. Furthermore, PBT yielded a better treatment response than did XRT. The

median overall survival (OS) for PBT and XRT patients was 31 and 14 months, respectively, and the 24-month OS for PBT and XRT patients was 59.1% and 28.6%, respectively [30]. According to a retrospective analysis of 22 patients with large liver tumors (median size 11 cm), PBT was effective, yielding a tumor control rate of 87% at 2 years, with significant toxicity [31]. In our previous study, we used a murine orthotopic HCC tumor model to investigate the effectiveness of XRT in inhibiting tumor progression, metabolism, and water molecular diffusion [10]. XRT with a 15 Gy dose reduced the tumor size on day 13. In comparison, in this study, significant tumor reduction was observed as early as day 7 after 20 Gy PBT. [18F]-FDG PET scans showed no significant change in SUVs in tumors within one week, regardless of treatment with XRT or PBT, an effect attributed to suppressed tumor proliferation at an early stage.

The early biological response of PBT

Few preclinical studies have reported on the response of liver tumors to PBT. Recently, Chen et al. reported that PBT increased the level of programmed cell death ligand 1 (PD-L1) expression in tumor cells and recruited myeloid-derived suppressor cells (MDSCs), indicating that PBT has an immunomodulatory effect on the tumor microenvironment. More importantly, the combination of PBT with anti-PD-L1 treatment resulted in a much longer tumor growth delay than did PBT alone [32]. Furthermore, Chen et al. reported that in the peritumoral region of human HCC, enhanced glycolysis regulates tumor-associated macrophages with protumor activities by upregulating a key glycolytic enzyme, PFKFB3 [33]. Our study revealed an increase in the number of macrophages infiltrating tumors from day 1 to day 7 after PBT. Additionally, a rebound in glycolysis and proliferation was observed in BNL tumors 7 days after receiving 20 Gy PBT. Therefore, the immune response induced by PBT may play a partial role in enhancing tumor glycolysis.

To our knowledge, few studies have been published that assessed the biological response to proton therapy using imaging techniques. One study published by Brasse et al. compared [18F]-FDG and 3′-[18F]-fluoro-3′-deoxythymidine PET imaging biomarkers from a longitudinal follow-up of mice bearing SK-HEP-1 immortal human liver sinusoidal endothelial tumors after 20 Gy PBT [34]. The decreased [18F]-FDG uptake was correlated with the cell proliferation marker Ki-67 and was observed after PBT irradiation on day 3, which is consistent with our results. However, depending on the cell type, we observed different effects on tumor growth. After 20 Gy PBT, the proliferation rate of SK-HEP-1 tumors significantly decreased within 20 days, while that of BNL tumors rebounded in just 7 days. These results suggest differential intrinsic radiosensitivity to protons between the two HCC tumor cell lines, which might also affect FDG uptake.

Limitations of dynamic [18F]-FDG PET

Dynamic whole-body (DWB) PET/CT has gained significant attention in recent years and can potentially be incorporated into routine clinical practice [16, 35]. The initial pilot results for DWB PET/CT have indicated that kinetic PET parameters are a promising addition to the gold standard quantitative SUV parameter in oncological studies. However, optimal acquisition protocols, data processing, and technical complexities are currently challenging during routine scans. The parameters obtained from in vivo kinetic modeling studies are crucial for validating initial strategies for diagnosis, prediction, and treatment response evaluations [36]. However, there are still several limitations of in vivo dynamic FDG PET studies. Blood sampling is the gold standard for kinetic modeling analysis, and it is used to obtain arterial input function. However, blood sampling methods, such as blood vessel catheterization and animal survival, are challenging. Therefore, IDIF was implemented in our study as well as in other published studies [11, 37]; however, IDIF can impact image spatial resolution, partial volume correction, and temporal resolution. In our study, the signal from the abdominal artery/vein was measured via IDIF with a voxel size of 0.4 mm × 0.4 mm × 0.4 mm. The thickness of the abdominal artery was approximately 1 mm, as measured by T2-weighted imaging, indicating that spatial resolution was relatively close to the target vessel size. The goodness of fit for the IDIF from the abdominal artery/vein was 0.90 ± 0.06 ($n = 12$), with an AIC value of 50.89 ± 13.64 ($n = 12$). These results suggest a reasonably good modeling performance. In comparison, Tao Wang et al. reported a higher AIC value (80.92 ± 29.44) in a clinical hepatocellular carcinoma PET study using a dual-input model [38], while Kathrine Røe et al. reported a median goodness of fit of 0.97 using IDIF in a mouse prostate cancer model [11].

Although our results are within an acceptable range for preclinical studies, the slightly lower goodness of fit may be due to the limited image resolution of our PET system, especially given the small diameter of mouse vasculature. Partial volume effects and IDIF signal contamination from surrounding tissues could contribute to reduced fitting precision. Therefore, future enhancements in spatial resolution or hybrid PET/MRI-guided localization may further improve modeling accuracy and IDIF performance. Furthermore, to acquire a sufficient signal from IDIF, the temporal resolution in our study was 10 s per frame, ensuring a distinguishable and consistent peak shape. We did not evaluate shorter time frames, but such optimization could also enhance IDIF accuracy. The optimization of IDIF will be our next step.

Future directions

PBT is a newer type of radiation treatment that is effective, especially for treating HCC [7], head and neck tumors [39], and pediatric cancers [40]. It is becoming increasingly popular worldwide. Compared to conventional photon therapy, PBT offers a better dose distribution, which reduces the amount of healthy tissue exposed to radiation. This leads to better treatment outcomes and an improved quality of life for patients. However, PBT is more expensive than conventional photon therapy, although this increased cost may be offset by the benefits of avoiding long-term radiation-related side effects. In this proof-of-concept study, we demonstrated the utility of multimodal imaging in evaluating the biological impact of PBT in a preclinical tumor model. Following 20 Gy PBT, we observed increased water diffusion (ADC value: 1.2 folds) and blood perfusion (K1 value: 1.7 folds) in the HCC tumor microenvironment as early as day 3, with these changes persisting through day 7. Notably, however, a rebound in tumor glycolysis and proliferation was also detected by day 7 (Glut1: 2.37 folds; Ki-67: 0.86 folds), suggesting a potential window for therapeutic intervention. These findings imply that combining PBT with targeted therapies, such as anti-angiogenic agents, glycolysis inhibitors (e.g., 2-deoxy-D-glucose) [41], or anti-proliferative drugs, may enhance therapeutic efficacy when administered early during treatment.

Building upon this platform, future research will explore clinically relevant PBT strategies, including hypofractionation and potential FLASH radiotherapy effects, and assess their biological responses. Additionally, systematic evaluation of varying proton doses and consistent analysis of LETd in both in vivo and in vitro models will be critical to advancing our understanding of the relative biological effectiveness of PBT. Ultimately, these efforts aim to optimize PBT-based treatment regimens and explore rational combination therapies for improved HCC management.

Conclusion

The use of SUVs derived from [18F]-FDG PET appears to be a very promising imaging tool for monitoring the growth of BNL-HCC tumors. Based on longitudinal scans, dynamic [18F]-FDG PET and DWI MRI techniques provide complementary information on the tumor response to PBT within 7 days, showing increased perfusion and water molecular diffusion over time. Notably, the glycolysis and immune responses in tumors were induced, while the proliferation rebounded 7 days after PBT. Overall, molecular functional imaging seems to be an effective tool for early assessment of the effects of PBT, providing strong evidence for combination therapy with systemic drugs such as anti-glycolysis or anti-proliferation drugs and PBT.

Abbreviations

ADC	Apparent diffusion coefficient
DWI	Diffusion-weighted imaging
DWB	Dynamic whole-body
FDG	Fluorodeoxyglucose
Glut1	Glucose transporter 1
H&E	Hematoxylin and eosin
HCC	Hepatocellular carcinoma
HK1	Hexokinase 1
IDIF	Image-derived input function
IHC	Immunohistochemistry
IF	Immunofluorescence
LETd	Dose-averaged linear energy transfer
MRI	Magnetic resonance imaging
OS	Overall survival
PET	Positron emission tomography
PD-L1	Programmed cell death ligand 1
PBT	Proton beam therapy
XRT	X-ray treatment
SOBP	Spread-out Bragg peak
SUV	Standardized uptake value
ROIs	Region of interests

Supplementary Information

The online version contains supplementary material available at https://doi.org/10.1186/s13014-025-02673-0.

Supplementary Material 1: **Supplemental data 1**. The installation of proton beam therapy and the dose profile in the field of view. a. The setup for the mice that received proton beam therapy. (a) Mice receiving proton beam therapy, with the red cross centered on the HCC tumor on the liver. (b) The 10-mm square field of view covers 85–90% of the 20 Gy PBT dose profile. **Supplemental data 2**. There were no notable differences in the relative ki or k3 values between the PBT and non-PBT groups on the indicated days. When comparing the changes in time points for the PBT group, ki and k3 on day 1 after PBT decreased by 34% and 29%, respectively, compared to the baseline values. The k3 values remained similar from day 1 to day 7 after PBT.

Acknowledgements

Authors thank Laboratory Animal Center and Radiation Research Core Laboratory, Chang Gung Memorial Hospital, Linkou, for molecular imaging and technical support.

Author contributions

Y.H.C., C.C.W., G.L., C.FY. and F.H.C. contributed to the study conception and design. Material preparation, data collection and analysis were performed by Y.H.C., I.C.C. and F.J. The first draft of the manuscript was written by Y.H.C. and all authors commented on previous versions of the manuscript. All authors read and approved the final manuscript.

Funding

We received funding support from Ministry of Science and Technology [Grant MOST 111-2314-B-182 A-011-MY2], Chang Gung Medical Foundation (Taiwan) [Grants CMRPG3N0461-62] by Yi-Hsiu Chung; [Grants NSTC 112-2314-B-182-054-MY3], Chang Gung University [Grants UMRPD1N0061] by Ching-Fang Yu.

Data availability

No datasets were generated or analysed during the current study.

Declarations

Ethics approval and consent to participate

We confirm that all methods were carried out in accordance with relevant guidelines and regulations. All animal proton irradiation and in vivo image acquisition protocols followed the animal guidelines established and approved by the Institutional Animal Care and Use Committee of Chang Gung

Memorial Hospital, Taiwan (IACUC 2022010302). All the authors confirmed that the study was carried out in compliance with the ARRIVE guidelines.

Consent for publication
Not applicable.

Competing interests
The authors declare no competing interests.

Author details
[1]Department of Medical Research and Development, Research Division, Chang Gung Memorial Hospital at Linkou, Taoyuan 333011, Taiwan
[2]Research Center for Radiation Medicine, Chang Gung University, Taoyuan 333323, Taiwan
[3]Radiation Research Core Laboratory, Linkou Chang Gung Memorial Hospital, Taoyuan City 333011, Taiwan
[4]Department of Medical Imaging and Radiological Sciences, Chang Gung University, Taoyuan 333323, Taiwan
[5]Department of Medical Imaging and Intervention, Clinical Metabolomics Core, Institute for Radiological Research, Chang Gung Memorial Hospital at Linkou and Chang Gung University, Taoyuan 333423, Taiwan
[6]Department of Radiation Oncology, Chang Gung Memorial Hospital Linkou Branch,, Taoyuan 333011, Taiwan
[7]Institute of Nuclear Engineering and Science, National Tsing Hua University, Hsinchu 300044, Taiwan
[8]Department of Engineering and System Science, National Tsing Hua University, Hsinchu 300044, Taiwan

Received: 19 August 2024 / Accepted: 26 May 2025
Published online: 06 June 2025

References

1. Su TH, Wu CH, Liu TH, Ho CM, Liu CJ. Clinical practice guidelines and real-life practice in hepatocellular carcinoma: A Taiwan perspective. Clin Mol Hepatol. 2023;29(2):230–41.
2. Sung H, Ferlay J, Siegel RL, Laversanne M, Soerjomataram I, Jemal A, et al. Global Cancer statistics 2020: GLOBOCAN estimates of incidence and mortality worldwide for 36 cancers in 185 countries. CA Cancer J Clin. 2021;71(3):209–49.
3. PDQ Adult Treatment Editorial Board. Primary Liver Cancer Treatment (PDQ®): Health Professional Version. 2023.
4. Mohan R. A review of proton Therapy - Current status and future directions. Precis Radiat Oncol. 2022;6(2):164–76.
5. Lundkvist J, Ekman M, Ericsson SR, Jonsson B, Glimelius B. Proton therapy of cancer: potential clinical advantages and cost-effectiveness. Acta Oncol. 2005;44(8):850–61.
6. Cubillos-Mesias M, Baumann M, Troost EGC, Lohaus F, Lock S, Richter C, et al. Impact of robust treatment planning on single- and multi-field optimized plans for proton beam therapy of unilateral head and neck target volumes. Radiat Oncol. 2017;12(1):190.
7. Kobeissi JM, Hilal L, Simone CB 2nd, Lin H, Crane CH, Hajj C. Proton therapy in the management of hepatocellular carcinoma. Cancers (Basel). 2022;14(12).
8. Keener AB. Making radiation oncology more personal. Nature. 2020;585(7826):S10–2.
9. Chen FH, Wang CC, Liu HL, Fu SY, Yu CF, Chang C, et al. Decline of tumor vascular function as assessed by dynamic Contrast-Enhanced magnetic resonance imaging is associated with poor responses to radiation therapy and chemotherapy. Int J Radiat Oncol Biol Phys. 2016;95(5):1495–503.
10. Chung YH, Yu CF, Chiu SC, Chiu H, Hsu ST, Wu CR, et al. Diffusion-weighted MRI and (18)F-FDG PET correlation with immunity in early radiotherapy response in BNL hepatocellular carcinoma mouse model: timeline validation. Eur J Nucl Med Mol Imaging. 2019;46(8):1733–44.
11. Roe K, Aleksandersen TB, Kristian A, Nilsen LB, Seierstad T, Qu H, et al. Preclinical dynamic 18F-FDG PET - tumor characterization and radiotherapy response assessment by kinetic compartment analysis. Acta Oncol. 2010;49(7):914–21.
12. Nishino M. Tumor response assessment for precision Cancer therapy: response evaluation criteria in solid tumors and beyond. Am Soc Clin Oncol Educ Book. 2018;38:1019–29.
13. Ganesan R, Yoon SJ, Suk KT. Microbiome and metabolomics in liver cancer: scientific technology. Int J Mol Sci. 2022;24(1).
14. Wahl RL, Jacene H, Kasamon Y, Lodge MA. From RECIST to PERCIST: evolving considerations for PET response criteria in solid tumors. J Nucl Med. 2009;50(Suppl 1):S122–50.
15. Pinilla I, Rodríguez-Vigil B, Gómez-León N. Integrated FDG PET/CT: utility and applications in clinical oncology. Clin Med Oncol. 2008;2:181–98.
16. Dimitrakopoulou-Strauss A, Pan L, Sachpekidis C. Kinetic modeling and parametric imaging with dynamic PET for oncological applications: general considerations, current clinical applications, and future perspectives. Eur J Nucl Med Mol Imaging. 2021;48(1):21–39.
17. Sommariva S, Caviglia G, Sambuceti G, Piana M. Mathematical models for FDG kinetics in cancer: A review. Metabolites. 2021;11(8).
18. Kajary K, Lengyel Z, Tokes AM, Kulka J, Dank M, Tokes T. Dynamic FDG-PET/CT in the initial staging of primary breast cancer: clinicopathological correlations. Pathol Oncol Res. 2020;26(2):997–1006.
19. Kele PG, van der Jagt EJ. Diffusion weighted imaging in the liver. World J Gastroenterol. 2010;16(13):1567–76.
20. Lo CH, Huang WY, Hsiang CW, Lee MS, Lin CS, Yang JF, et al. Prognostic significance of apparent diffusion coefficient in hepatocellular carcinoma patients treated with stereotactic ablative radiotherapy. Sci Rep. 2019;9(1):14157.
21. Surov A, Eger KI, Potratz J, Gottschling S, Wienke A, Jechorek D. Apparent diffusion coefficient correlates with different histopathological features in several intrahepatic tumors. Eur Radiol. 2023;33(9):5955–64.
22. Paganetti H. Proton relative biological Effectiveness – Uncertainties and opportunities. Int J Part Therapy. 2018;5(1):2–14.
23. Brooks RA. Alternative formula for glucose utilization using labeled Deoxyglucose. J Nucl Med. 1982;23(6):538–9.
24. Chung YH, Hung TH, Yu CF, Tsai CK, Weng CC, Jhang F et al. Glycolytic plasticity of metastatic lung Cancer captured by noninvasive (18)F-FDG PET/CT and serum (1)H-NMR analysis: an orthotopic murine model study. Metabolites. 2023;13(1).
25. Arifin WN, Zahiruddin WM. Sample size calculation in animal studies using resource equation approach. Malays J Med Sci. 2017;24(5):101–5.
26. Van Schaftingen E. Hexokinases/Glucokinases. In: Lennarz WJ, Lane MD, editors. Encyclopedia of biological chemistry. New York: Elsevier; 2004. pp. 372–7.
27. Fliedner FP, Engel TB, El-Ali HH, Hansen AE, Kjaer A. Diffusion weighted magnetic resonance imaging (DW-MRI) as a non-invasive, tissue cellularity marker to monitor cancer treatment response. BMC Cancer. 2020;20(1):134.
28. Cohen AD, LaViolette PS, Prah M, Connelly J, Malkin MG, Rand SD, et al. Effects of perfusion on diffusion changes in human brain tumors. J Magn Reson Imaging. 2013;38(4):868–75.
29. Cheng JY, Liu CM, Wang YM, Hsu HC, Huang EY, Huang TT, et al. Proton versus photon radiotherapy for primary hepatocellular carcinoma: a propensity-matched analysis. Radiat Oncol. 2020;15(1):159.
30. Sanford NN, Pursley J, Noe B, Yeap BY, Goyal L, Clark JW, et al. Protons versus photons for unresectable hepatocellular carcinoma. Liver Decompensation and Overall Survival; 2019.
31. Sugahara S, Oshiro Y, Nakayama H, Fukuda K, Mizumoto M, Abei M, et al. Proton beam therapy for large hepatocellular carcinoma. Int J Radiat Oncol Biol Phys. 2010;76(2):460–6.
32. Chen MF, Chen PT, Hsieh CC, Wang CC. Effect of proton therapy on tumor cell killing and immune microenvironment for hepatocellular carcinoma. Cells. 2023;12(2).
33. Chen DP, Ning WR, Jiang ZZ, Peng ZP, Zhu LY, Zhuang SM, et al. Glycolytic activation of peritumoral monocytes fosters immune privilege via the PFKFB3-PD-L1 axis in human hepatocellular carcinoma. J Hepatol. 2019;71(2):333–43.
34. Brasse D, Burckel H, Marchand P, Rousseau M, Ouadi A, Vanstalle M, et al. Comparison of the [(18)F]-FDG and [(18)F]-FLT PET tracers in the evaluation of the preclinical proton therapy response in hepatocellular carcinoma. Mol Imaging Biol. 2021;23(5):724–32.
35. Rahmim A, Lodge MA, Karakatsanis NA, Panin VY, Zhou Y, McMillan A, et al. Dynamic whole-body PET imaging: principles, potentials and applications. Eur J Nucl Med Mol Imaging. 2019;46(2):501–18.
36. Wimberley C, Nguyen DL, Truillet C, Peyronneau MA, Gulhan Z, Tonietto M, et al. Longitudinal mouse-PET imaging: a reliable method for estimating binding parameters without a reference region or blood sampling. Eur J Nucl Med Mol Imaging. 2020;47(11):2589–601.

37. Wang J, Shao Y, Liu B, Wang X, Geist BK, Li X, et al. Dynamic (18)F-FDG PET imaging of liver lesions: evaluation of a two-tissue compartment model with dual blood input function. BMC Med Imaging. 2021;21(1):90.
38. Wang T, Deng Y, Wang S, He J, Wang S. Kinetic (18)F-FDG PET/CT imaging of hepatocellular carcinoma: a dual input four-compartment model. EJNMMI Phys. 2024;11(1):20.
39. Nuyts S, Bollen H, Ng SP, Corry J, Eisbruch A, Mendenhall WM et al. Proton therapy for squamous cell carcinoma of the head and neck: early clinical experience and current challenges. Cancers (Basel). 2022;14(11).
40. Thomas H, Timmermann B. Paediatric proton therapy. Br J Radiol. 2020;93(1107):20190601.
41. Sasaki K, Nishina S, Yamauchi A, Fukuda K, Hara Y, Yamamura M, et al. Nanoparticle-Mediated delivery of 2-Deoxy-D-Glucose induces antitumor immunity and cytotoxicity in liver tumors in mice. Cell Mol Gastroenterol Hepatol. 2021;11(3):739–62.

Publisher's note